Materials Characterization 195 (2023) 112486

Contents lists available at ScienceDirect

Materials Characterization

journal homepage: www.elsevier.com/locate/matchar

Effect of low-temperature precipitates on microstructure and pseudoelasticity of an Fe–Mn–Si-based shape memory alloy

Hesamodin Khodaverdi [a], Maryam Mohri [b,*], Amir Sabet Ghorabaei [a], Elyas Ghafoori [b,c], Mahmoud Nili-Ahmadabadi [a,*]

[a] School of Metallurgy and Materials Engineering, College of Engineering, University of Tehran, Tehran, Iran
[b] Empa, Swiss Federal Laboratories for Materials Science and Technology, 8600 Dübendorf, Switzerland
[c] Institute for Steel Construction, Faculty of Civil Engineering and Geodetic Science, Leibniz University Hannover, 30167 Hannover, Germany

ARTICLE INFO

Keywords:
Fe–Mn–Si-based shape memory alloy
Superelasticity
Precipitation
Equilibrium phase diagram
Transmission electron microscopy

ABSTRACT

Fe–Mn–Si-based shape memory alloys (Fe-SMAs) have attracted much research attention due to their potential applications for vibration mitigation, energy dissipation, and re-centering in the construction sector. Because of the crucial impact of precipitation on the pseudoelasticity (PE) behavior of Fe-SMAs, the equilibrium phase diagram of an Fe–17Mn–5Si–10Cr–4Ni–1(V-C) (wt%) SMA was used in this study to identify a low-temperature precipitate and study its effect on the microstructure and PE of the alloy after a low-temperature aging process. Transmission electron microscopy (TEM) studies revealed that aging at 485 °C for 6 h after aging at 750 °C for 6 h led to the precipitation of fresh, parallelogram-shaped, (Cr–V–C)-rich precipitates along with elliptical-shaped, V-rich precipitates in the austenite grains of the recrystallized samples. Numerous parallel stacking faults (SFs) were formed due to the presence of the precipitates within the austenite grains. It is postulated that such an arrangement of SFs can further improve the PE by reducing the activation energy for the nucleation of ε-martensite laths and inhibiting them from colliding with each other and consequent formation of α'-martensite, resulting in a residual strain reduction to 2.7% after 4.0% tensile straining.

1. Introduction

Fe–Mn–Si-based shape memory alloys (SMAs), as one of the most practical categories of Fe-based SMAs, have attracted much research attention [1–4]. Due to their low material cost, high Young's modulus and strength, exceptional workability, and high stress and strain recovery [5,6], these alloys have been used for a wide range of applications such as coupling devices [7], mechanical tightening, structural elements, active controls, pre-stressing or post-tensioning of structures [8], and damping devices [9]. However, low pseudoelasticity (PE) has prevented them from being used in many applications such as dissipative re-centering systems in civil engineering [10].

A new design for Fe-based SMAs, Fe–17Mn–5Si–10Cr–4Ni–1(V-C) (wt%), has been developed in Swiss Federal Laboratories for Materials Science and Technology (Empa) [11–15]. The alloy can be produced by a relatively cheap casting process under atmospheric conditions [16] and has high potential for large-scale repair and strengthening in the construction section [17] and passive vibration damping [18].

A combination of the reversible motion of Shockley partial dislocations (SPDs) and back transformation from ε-martensite (with hexagonal close-packed (HCP) lattice structure) to γ-austenite (with face-centered cubic (FCC) lattice structure) in unloading is believed to be the microstructural reason for the PE effect in Fe–Mn–Si-based SMAs [19]. Several attempts have been made to enhance the PE of Fe–Mn–Si-based SMAs, such as controlling the grain size [20,21], texturizing, and precipitation [22] in combination with stacking fault energy (SFE) control [23]. Among the different approaches, SFE control and precipitation have had a greater impact on PE improvement. Precipitates such as $Cr_{23}C_6$ [24], TiC [25], VN [26], VC [27], and NbC [28] are used for PE improvement.

It has been revealed that NbC carbides increase the strength of the γ-austenite phase and assist in the reversible movement of the γ/ε interfaces through a specific crystallographic path. The back-stress on the growing ε-martensite lath due to the stress fields induced by the NbC carbides causes this back transformation [28,29]. In addition, VC precipitates promote the formation of ε-martensite by reducing the critical resolved shear stress (CRSS) of austenite [19]. Precipitates also increase

* Corresponding authors.
E-mail addresses: maryam.mohri@empa.ch (M. Mohri), nili@ut.ac.ir (M. Nili-Ahmadabadi).

https://doi.org/10.1016/j.matchar.2022.112486
Received 26 August 2022; Received in revised form 10 November 2022; Accepted 12 November 2022
Available online 17 November 2022
1044-5803/© 2022 The Authors. Published by Elsevier Inc. This is an open access article under the CC BY license (http://creativecommons.org/licenses/by/4.0/).

the number of dislocations and stacking faults (SFs) in the γ-austenite matrix, which act as embryos for ε-martensite nucleation [30–34]. It has recently been found that having a fine-grained austenite matrix along with uniform distribution of precipitates facilitates the γ ⇌ ε transformation and enhances the PE behavior of the alloy [35].

In a recent study on the newly designed Fe–Mn–Si-based SMA [36], it has been shown that (Cr–V–C)-rich precipitates uniformly form inside the austenite grains by high-temperature aging at 750 °C, resulting in a significant improvement of PE. To recognize any new low-temperature precipitates, it is essential to investigate the equilibrium phase diagram of the alloy. In the present work, the effect of low-temperature aging at 485 °C on the evolution of a new type of precipitate is studied, and its combination with the primary high-temperature precipitates is employed to further enhance the PE of the alloy. Low-temperature precipitates, which may improve shape memory and superelasticity properties, are highly desirable because lowering the aging temperature decreases manufacturing costs and associated problems like oxidation and grain growth. It is shown that after 4.0% loading in tension, a residual strain of 2.7% can be achieved. The underlying mechanisms of the observed improvement in PE after low-temperature aging at 485 °C are studied by detailed microstructural characterizations, which provide new insights into the processing of this alloy for vibration mitigation and seismic damping applications.

2. Materials and methods

Rebars with a diameter of 18 mm and a nominal composition of Fe–17Mn–5Si–10Cr–4Ni–1(V-C) (wt%), provided by re-fer AG, Switzerland, were used in this study. The material was produced by hot rolling at 1000 °C after casting. The microstructure of the as-received rebars consisted of equiaxed austenite grains and fine precipitates at the grain boundaries [35]. The as-received alloy was cold–caliber-rolled to an octagonal-shaped speciemen with equal sides of 14.2 mm. The cold rolling was performed in 16 consecutive steps to reach an equivalent strain of 0.25 at ambient temperature, using a caliber rolling machine with a roller diameter of 110 mm and a rolling speed of 800 mm/min. The cold-rolled specimens were recrystallized in a vacuum furnace at 925 °C for 50 min followed by air cooling to room temperature [35]. High-temperature aging was performed on the recrystallized specimens at 750 °C for 6 h in a muffle furnace followed by air cooling to ambient tempearture. Subsequently, a set of the aged specimens was double aged at a relatively lower temperature of 485 °C for 6 h and then cooled down to the room temperature under atmospheric conditions. The recrystallized, single aged, and double aged specimens are hereafter named as Rex, Rex-Aged, and Rex-Double aged, respectively.

Dilatometry analysis with a cooling/heating rate of 1 °C/s was conducted on cylindrical samples with a length of 10 mm and a diameter of up to 2 mm in an Adamel DT1000 dilatometer. A schematic view of the heat treatment cycles and the optical microstructures of the as-received material before and after the cold rolling are provided in the Supplementary Material File (see Fig. S1).

The volume fractions of phase constituents were measured using X-ray diffraction (XRD) analysis with a Cu Kα radiation source (λ = 0.154 nm) at an acceleration voltage of 45 kV and a tube current of 200 mA. The microstructures of the specimens were studied using optical microscopy (OM; ZEISS Axioskop 2 MAT), secondary electron analysis by field-emission scanning electron microscopy (FE-SEM; FEI Nova NanoSEM 450), and high-resolution transmission electron microscopy (HR-TEM; FEI Tecnai F20 series). The chemical compositions of precipitates were analyzed using energy-dispersive X-ray spectroscopy (EDS; Oxford X-Max^N 80 T silicon drift detector with a take-off angle of 14.6° and a resolution of 134 eV FWHM at reference energy of 5.9 keV) by the TEM. Standard samples of pure elements were used for calibrating the TEM imaging and analysis (TIA) interface of the microscope software. Moreover, the multi-polynomial background correction for the X-ray signals along with thin foil thickness correction for the TEM specimens was considered to analyze K_α radiation of the alloying elements. The EDS spectra were quantified by the TIA software based on the Cliff-Lorimer method [37] with k-factors calculated with respect to silicon. A maximum relative uncertainty value of ~5% was detected for the reported chemical compositions. Samples for the OM and SEM observations were mechanically polished and etched with a solution of H_2O_2 (35%), HNO_3 (65%), and HCl (32%) (7:30:9). The HR-TEM specimens were prepared by standard mechanical thinning followed by electropolishing in a solution of $HClO_4$ and C_2H_5OH (1:9) at −20 °C and 22 V.

To evaluate the mechanical properties of the heat-treated samples, monotonic loading–unloading experiments were performed with a Zwick/Roell Z020 tensile test machine. During the loading–unloading tests, the strain evolution was measured with a calibrated sensor-arm extensometer type BTC-EXMULTI.011 made by Zwick/Roell Company. Longitudinal tensile specimens were machined from the samples and prepared in a dog-bone shape with a reduced section length of 32.0 mm and a cross-section of 1.0 × 0.8 mm^2 (Fig. 1). Furthermore, to study the microstructural evolution of the samples after loading–unloading tests, sub-size tensile specimens with a gauge length of 25.00 mm and a width of 6.25 mm were prepared according to the ASTM E8M-04 standard. Tensile loading to a maximum strain of 4% was carried out at room temperature with a crosshead speed of 0.5 mm/min followed by unloading with the same crosshead speed until a force of 10 N was attained.

3. Results

3.1. Equilibrium phase diagram of Fe–17Mn–5Si–10Cr–4Ni–1(V-C) (wt %) alloy

Fig. 2 shows the equilibrium phase diagram of the studied alloy calculated by using Thermo-Calc software with TCFE7 database [38]. The liquid phase is thermodynamically stable at high temperatures down to approximately 1320 °C, where it starts to solidify to form the γ-austenite phase in a temperature range of about 95 °C until 1225 °C. Further cooling to 1000 °C promotes the formation of M_7C_3 carbide via a precipitation reaction of $\gamma \rightarrow \gamma + M_7C_3$. Subsequently, the Sigma1 phase is formed by a precipitation reaction of γ → γ + Sigma1 at 665 °C, and its molar fraction reaches a maximum of ~0.15 at 485 °C (inset of Fig. 2). Additionally, the thermodynamic calculations predict that the Sigma1 phase transforms into the Sigma2 and A2 phases below 485 °C. In the present study, the possible precipitation of the Sigma1 phase and its relation to PE evolution were investigated through double aging of the Rex-Aged samples at 485 °C.

3.2. Microstructure development after high- and low-temperature aging

Figs. 3a–c show the FE-SEM micrographs of the Rex (a), Rex-Aged (b), and Rex-Double aged (c) samples. The microstructure of the Rex sample mainly consisted of recrystallized austenite grains with an average grain size of 5 μm and reversed austenite regions with a diameter of approximately 1 μm. Since grain boundary junctions act as preferential nucleation sites for the martensitic transformation, most strain-induced martensite forms in these locations [39]. Therefore, the reversed austenite grains usually appeared in the triple junctions of recrystallized austenite grains (Fig. 3a). Such formation of reversed

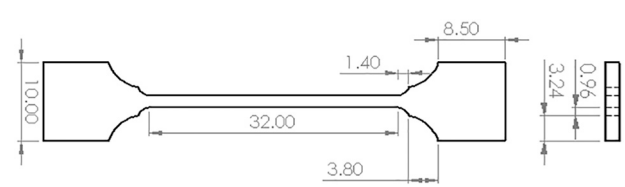

Fig. 1. Geometry of the dog-bone specimens used for the tensile tests (dimensions in mm).

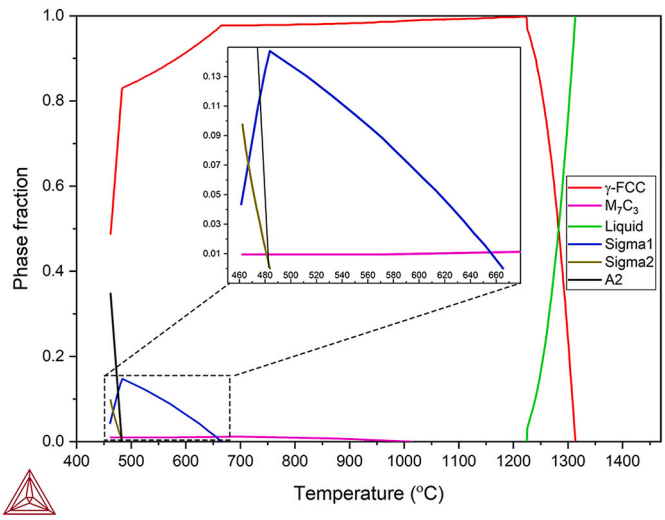

Fig. 2. Calculated equilibrium phase diagram of the studied Fe–17Mn–5Si–10Cr–4Ni–1(V-C) (wt%) alloy at 1 atm pressure by the Thermo-Calc software.

austenite at the triple junctions of recrystallized austenite grains during the annealing of cold-rolled austenite has also been reported elsewhere [39,40]. Moreover, there were some constituents with sizes of less than 800 nm located inside the austenite grains and also at the grain boundaries of austenite, which were (Cr–V–C)-rich precipitates according to our previous findings [35]. In comparison to the Rex sample, the Rex-Aged sample showed a sharp increase in the number of precipitates with a higher volume fraction inside the austenite grains than at the grain boundaries. The average austenite grain size of the Rex sample remained close to 5 μm after aging (Fig. 3b). After low-temperature aging of the Rex-Aged sample at 485 °C for 6 h, the volume fraction and continuity of reversed austenite regions decreased (Fig. 3c). In addition, the number of (Cr–V–C)-rich precipitates (polyhedral-shaped) was reduced, but some new needle-shaped precipitates formed inside the austenite grains. Similar to the Rex and Rex-Aged samples, the grain size of recrystallized austenite for the Rex-Double aged sample did not change, but the grain size of reversed austenite slightly decreased (Fig. 3c).

Fig. 3d illustrates the XRD diffractograms of the specimens from which the volume fractions of α'-martensite and ε-martensite were calculated according to the method provided in Ref. [41]. The Rex sample contained 14 vol% ε-martensite and 7.9 vol% α'-martensite, while the Rex-Aged sample possessed a much higher volume fraction of ε-martensite of about 43% and, interestingly, had almost zero volume fraction of α'-martensite. The disappearance of α'-martensite and the increase in the volume fraction of ε-martensite in the Rex-Aged specimen could be related to the formation of precipitates, which can change the chemical composition of the austenite matrix and inhibit the formation of randomly oriented ε-martensite laths inside the austenite grains [42]. Furthermore, the XRD diffractogram of the Rex-Aged sample showed peak splitting (indicated by the small arrow in Fig. 3d), which can be related to the presence of precipitates, SFs, and ε-martensite that reduce the symmetry of the microstructure [43]. In comparison to the Rex-Aged sample, the volume fraction of ε-martensite reduced to nearly 16% and the degree of peak splitting decreased for the Rex-Double aged sample.

3.3. Loading–unloading experiments

The engineering stress-strain curves after loading–unloading tests for the As-Received aged [35] and the heat-treated samples are shown in Fig. 4. The values of PE and other tensile properties of the samples inferred from Fig. 4 are summarized in Table 1. For this particular alloy, the 0.1% offset yield stress ($\sigma_{Y0.1\%}$) was considered for estimating the onset stress of the martensitic transformation [44]. The elastic modulus of this alloy can vary between 40 and 170 GPa under different microstructural conditions [45]. Since the elastic moduli of the samples were

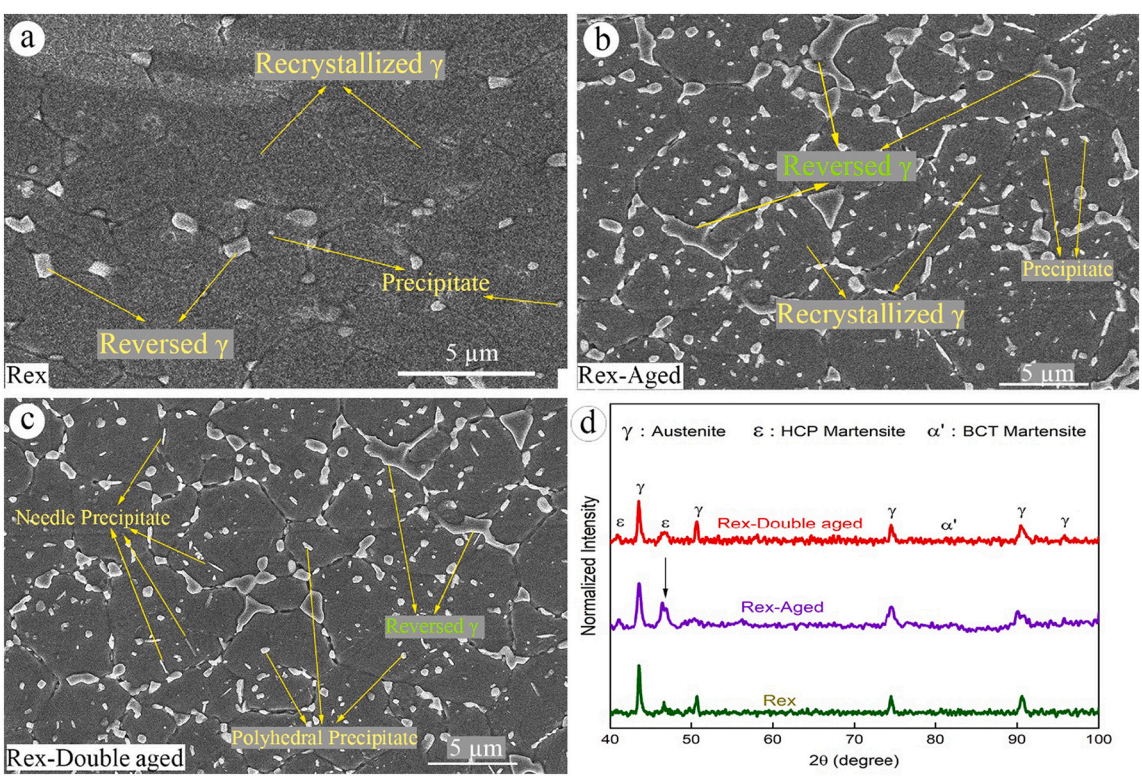

Fig. 3. SEM micrograph of the (a) Rex, (b) Rex-Aged, and (c) Rex-Double aged samples. (d) XRD diffractograms of the specimens.

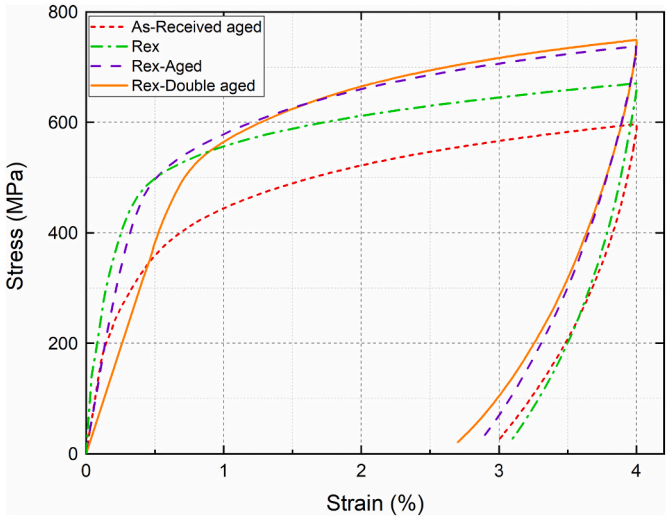

Fig. 4. Loading–unloading curves of the As-Received aged [35], Rex, Rex-Aged, and Rex-Double aged samples strained to 4% in tension.

calculated by using Hooke's law, the calculated values corresponded to mixed microstructures of austenite, ε-martensite, and α'-martensite with different volume fractions of the constituents. Furthermore, it has been shown that mainly the stress-induced martensitic transformation occurs until the stress level reaches the yielding point of this alloy [44]. Therefore, the mixture of phases is changed by increasing (decreasing) the strain in the elastic part, which justifies the nonlinear deformation behavior during loading (unloading). The PE strain was calculated according to Eq. (1):

$$\varepsilon_{total} = \varepsilon_{res} + \varepsilon_{pse} + \varepsilon_E = \varepsilon_{res} + \varepsilon_{pse} + \frac{\sigma_{4\%}}{E_{unloading}} \quad (1)$$

where ε_{res}, ε_{pse}, and ε_E are the residual strain, PE strain, and elastic strain, respectively. $\sigma_{4\%}$ denotes the strength at the peak tensile strain, and $E_{unloading}$ is the elastic modulus in unloading.

The Rex sample exhibited an elastic modulus of 160 GPa in loading which decreased to 105 and 80 GPa for the Rex-Aged and Rex-Double aged samples, respectively. The value of $\sigma_{Y0.1\%}$ was 440 MPa for the Rex sample, while it slightly increased and reached 475 MPa for the Rex-Aged sample. After performing the aging heat treatment at 485 °C for 6 h, the $\sigma_{Y0.1\%}$ increased to 525 MPa for the Rex-Double aged sample. Similarly, the $\sigma_{4\%}$ increased from 670 MPa for the Rex sample to 737 and 750 MPa for the Rex-Aged and Rex-Double aged samples, respectively. Furthermore, in comparison to the Rex sample with a residual strain of 3.09%, the Rex-Aged and Rex-Double aged samples showed relatively lower residual strains of 2.87% and 2.70%, respectively. Such behavior could be mainly related to the higher $\sigma_{4\%}$ values, lower Young's moduli and higher PE strains of the aged samples compared with those of the Rex sample (Table 1 and Eq. (1)). It is worth mentioning that the obtained residual strain of 2.70% for the Rex-Double aged samples after 4% loading in tension is the lowest residual strain value reported so far for this particular alloy.

3.4. TEM study on the microstructures after aging at high and low temperatures

Figs. 5a–b show TEM images from the substructure of the Rex sample. Particles with sizes between 15 and 20 nm were uniformly distributed in the austenite matrix (white arrows in Fig. 5a). It has recently been indicated that these particles are rich in vanadium and can be considered as embryos for the V-rich precipitates [35]. Additionally, a number of parallel SFs (blue arrows in Figs. 5a–b) could be observed in the microstructure of the Rex sample. The TEM images of the Rex-Aged sample are shown in Figs. 5c–d, indicating the formation of a higher number of SFs and ε-martensite laths after aging in comparison to the Rex sample. The TEM-EDS analysis showed that the polyhedral-shaped precipitates were rich in Cr, V and C elements (Fig. 5c). These particles with approximately similar chemical compositions but with spherical morphologies and relatively smaller sizes were also present in the substructure of the Rex sample (white arrows in Fig. 5b). The details of TEM-EDS analyses are provided in the Supplementary Material File (Figs. S2–S9). A dark-field TEM image obtained from the $[01\bar{1}0]$ reflection of ε-martensite is shown in the inset of Fig. 5d. It was observed that ε-martensite laths generally grew parallel to each other in separate groups in the samples.

Figs. 6a–d illustrate TEM images from the substructure of the Rex-Double aged sample. Fig. 6a shows an austenite grain with a large number of SFs that are all located in the same orientation inside the grain. Such a parallel orientation of SFs, but with a lower degree of orientation, was also detected in the TEM micrographs of the Rex and Rex-Aged samples (Fig. 5). In contrast to the other samples, parallelogram-shaped precipitates were observed in addition to polyhedral-shaped precipitates in the microstructure of the Rex-Double aged sample (Figs. 6b–c). As shown in the inset of Fig. 6c, the parallelogram-shaped precipitates indicated a range of 170–330 nm in length. It seemed that these precipitates were the same as the needle-shaped precipitates observed in the FE-SEM image (Fig. 3c), which a portion of their cross-section could be seen in the TEM images (Figs. 6b–c). Furthermore, ε-martensite laths with a limited number of variants were observed in the Rex-Double aged sample (Fig. 6b). An HR-TEM image from a section of one of the ε-martensite laths with a width of nearly 2.2 nm is shown in Fig. 6d. By applying the fast Fourier transform (FFT) and then the inverse FFT (IFFT) to a portion of the image (dashed white square), the displacement of atomic planes for the formation of ε-martensite from γ-austenite was revealed as shown with red lines in the inset of Fig. 6d.

Figs. 7a–b show TEM micrographs from the substructure of the Rex-Double aged sample after performing a loading–unloading test to a peak strain of 2% in tension. Unlike the substructures of the non-deformed samples (Figs. 5 and 6), parallel SFs crossed each other after applying the deformation (blue arrows in Fig. 7a). Moreover, the crossing SFs were trapped by the polyhedral-shaped, (Cr–V–C)-rich precipitates, resulting in the formation of highly distorted areas around the precipitates in the austenite matrix (yellow arrows in Fig. 7a). Fig. 7b indicates sparse V-rich precipitates, ranging from 70 to115 nm in size, inside a variant of annealing twins in the austenite phase. No SFs were observed in the twinned crystals that could tangle around the elliptical-shaped, V-rich precipitates, compared with the polyhedral-shaped

Table 1
Mechanical characteristics of the As-Received aged [35], Rex, Rex-Aged, and Rex-Double aged samples after loading–unloading experiments with a peak strain of 4% in tension. ε_{res}: residual strain, ε_{pse}: PE strain, ε_E: elastic strain, $\sigma_{Y0.1\%}$: 0.1% offset yield stress, $\sigma_{4\%}$: strength at peak tensile strain, $E_{loading}$: elastic modulus in loading, $E_{unloading}$: elastic modulus in unloading.

Sample name	$E_{loading}$ (GPa)	$\sigma_{Y0.1\%}$ (Mpa)	$\sigma_{4\%}$ (Mpa)	$E_{unloading}$ (GPa)	ε_E (%)	ε_{pse} (%)	ε_{res} (%)
As-Received aged [35]	160	275	600	130	0.46	0.54	3
Rex	160	440	670	135	0.50	0.41	3.09
Rex-Aged	105	475	737	115	0.64	0.49	2.87
Rex-Double aged	80	525	750	140	0.53	0.77	2.70

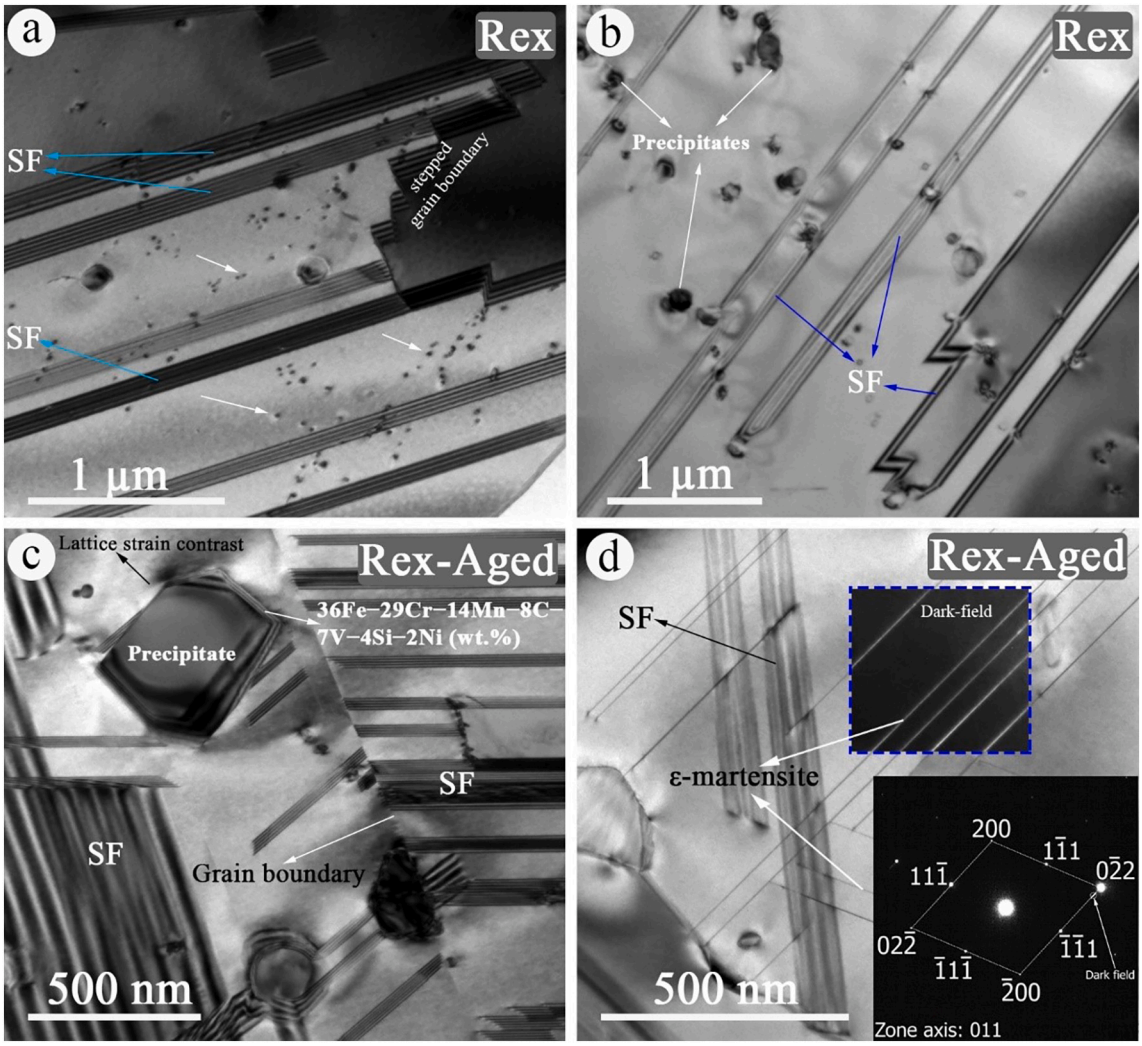

Fig. 5. (a–b) Bright-field TEM images of the Rex sample illustrating SFs and precipitates in the austenite matrix. (c) Bright-field TEM image of SFs and (Cr–V–C)-rich precipitates in the Rex-Aged sample. (d) Bright-field and dark-field TEM images from ε-martensite laths in the Rex-Aged sample; the [01$\bar{1}$0] reflection of ε-martensite was used for dark-field imaging as shown in the corresponding selected area electron diffraction pattern.

precipitates in the non-twinned regions. It was realized that these V-rich precipitates evolved from the fine particles observed in the Rex sample (Fig. 5a) such that their size increased at the expense of the reduction in their volume fraction by double aging the sample (Figs. 6a and 7b). Table 2 lists the reported chemical compositions of observed precipitates in several FeMnSi-SMAs subjected to different heat treatment conditions and the average chemical compositions of observed precipitates in this study.

4. Discussion

Several studies have investigated the mechanism of PE in Fe–Mn–Si-based SMAs. In the first attempts, Sawaguchi et al. [46] justified the PE behavior by the reverse transformation from ε-martensite to γ-austenite in unloading caused by the back-stress experienced by SPDs residing at the top of the ε-martensite plates. Leinenbach et al. [19] later showed that the microstructural reason for PE is a combination of the back transformation from ε-martensite to γ-austenite and reversible motions of SPDs. In low SFE materials, a dislocation typically can dissociate into two extended dislocations, creating an SF bounded by SPDs. Therefore, SFs play an important role in the PE response of the studied Fe–Mn–Si-based SMA with an SFE value of 5.75 mJ/m^2 [35].

Generally, the nucleation of ε-martensite in γ-austenite can be accomplished by forming SFs on (111) planes of the FCC crystal in every two layers at pre-existing SFs or as newly developing SFs [47,48]. Applying external stress will generate a dislocation loop two layers away from the existing SFs to produce a four-layer ε-martensite plate. When the thickness of the ε-martensite plate reaches a threshold value, a new martensite plate will then be formed at a certain distance to the first martensite plate to relax the lattice strain of the initially formed martensite plate. Therefore, the SFs are considered as embryos for the nucleation of ε-martensite [49,50]. It has also been reported that the essential factor for obtaining good PE behavior in Fe-based SMAs is the propensity to produce very thin ε-martensite plates by applying external stress [51]. Having a high density of SFs in the austenite grains is necessary to form extremely thin and single-variant ε-martensite plates with a uniform distribution within each grain of the austenite phase. Given the fact that α'-martensite, which weakens the PE behavior of Fe-based SMAs, can nucleate at the intersection of two ε-martensite laths [52], the formation of SFs in random orientations should be minimized in the microstructure.

Although the microstructure of the Rex specimen contains relatively equiaxed austenite grains with a small grain size, the tensile test does not show a significant PE response for this specimen (Figs. 3 and 4). The presence of 7.9 vol% α'-martensite in the microstructure is one of the reasons for this inferior PE behavior. Furthermore, the TEM images

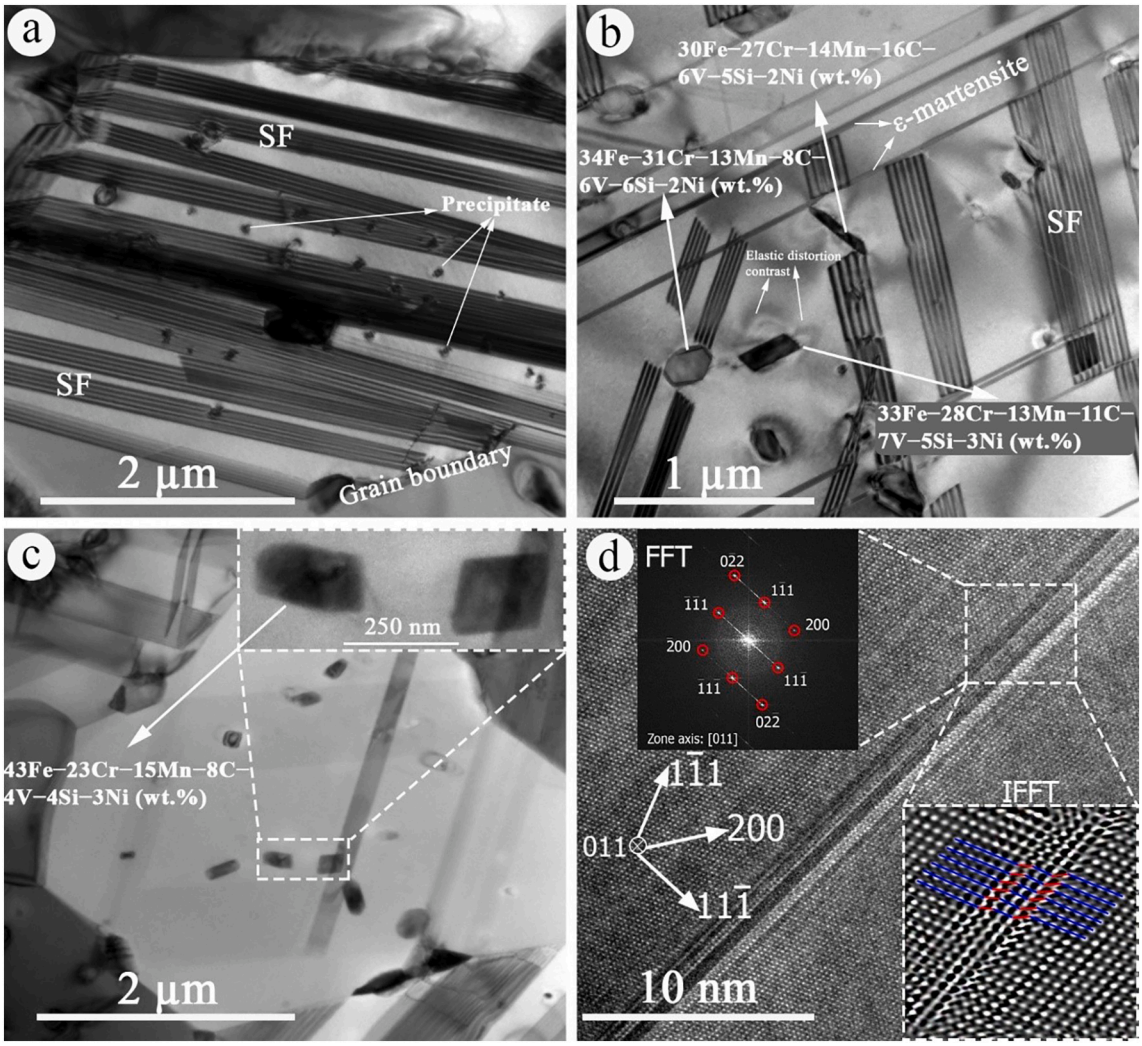

Fig. 6. Bright-field TEM images of the Rex-Double aged sample illustrating (a) a high number of parallel SFs in an austenite grain, (b) polyhedral- and parallelogram-shaped precipitates along with parallel SFs and ε-martensite laths in the austenite matrix, and (c) the distribution of parallelogram-shaped precipitates in the austenite matrix. (d) HR-TEM image and corresponding FFT and IFFT images of an ε-martensite lath formed parallel to the {111} planes of austenite. Selected lattice spots for producing the IFFT image are shown by the red circles in the FFT pattern. (For interpretation of the references to colour in this figure legend, the reader is referred to the web version of this article.)

show elliptical-shaped particles with a size of 15–20 nm in the microstructure of the Rex sample (Fig. 5a). Stanford et al. [53] have shown that fine particles with a size of less than 30 nm can be counterproductive to achieving superior PE behavior by pinning stress-induced ε-martensite and inhibiting its reversion to γ-austenite.

The ε_{res} value of the Rex-Aged sample (2.87%) shows about 7.1% improvement over that of the Rex sample (3.09%). This enhancement is mainly related to the more formation of (Cr–V–C)-rich precipitates inside the austenite grains with the same austenite grain size (5 μm) compared with the Rex sample. These polyhedral-shaped precipitates, which create lattice strains (Fig. 5c), are uniformly distributed in the austenite matrix (Fig. 3b), leading to the formation of a significant number of SFs accompanied by a high fraction (43 vol%) of ε-martensite (Figs. 5c–d). The high number of SFs not only facilitates the γ → ε martensitic transformation but also results in the significant reduction of Young's modulus compared with the Rex sample (Table 1). The reduction in Young's modulus is related to the change in the interatomic bonding configuration at the SFs [54].

In comparison to the ε_{pse} value of the Rex-Aged sample, an increase of 57% in ε_{pse} is observed for the Rex-Double aged sample, resulting in a higher PE strain of 0.77%. According to the equilibrium thermodynamic data at 485 °C (Fig. 2), sigma-type precipitates can form along with M_7C_3 carbides in the microstructure. By comparing these data with the precipitation behavior of the studied alloy at three different temperatures of 925, 750, and 485 °C (Figs. 5 and 6), the polyhedral-shaped and parallelogram-shaped precipitates in the Rex-Double aged sample could be related to M_7C_3-type and sigma-type precipitates in the phase diagram, respectively. Although there are some studies that support these arguments [55,56], the crystallography of the parallelogram-shaped precipitates with the average chemical composition of Fe–14Mn–5Si–26Cr–3Ni–6V–12C (wt%) needs to be investigated in detail in the future.

The observed improvement of ε_{pse} in the Rex-Double aged sample is thought to be partly caused by the formation of the new precipitates, which can induce the development of a higher number of SFs grouped in the same orientation inside the austenite grains compared with the other samples (Figs. 6a–b). The generation of a high number of precipitate/matrix interfaces in the double-aged sample can play a role in the formation of new SFs in the microstructure. It has been shown that dislocations form at the precipitate/matrix interface to accommodate the elastic strain fields (represented in Figs. 5c and 6b) accompanied by the formation of the precipitate [35,57]. Consequently, the SFs can be formed by the dissociation of the dislocations associated with the precipitate/matrix interface [58]. In addition, the formation of SFs after

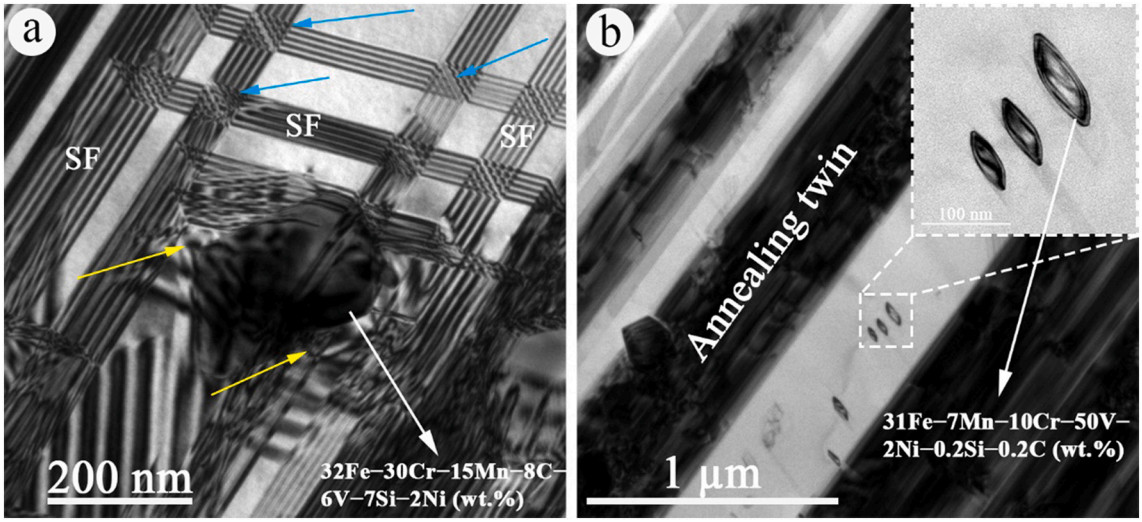

Fig. 7. Bright-field TEM images of the Rex-Double aged sample after a loading–unloading experiment to a peak strain of 2% in tension. (a) Groups of parallel SFs crossing each other (blue arrows) around a (Cr–V–C)-rich precipitate in non-twinned regions of the austenite matrix, creating distorted zones around the precipitate (yellow arrows). (b) Three elliptical-shaped, V-rich precipitates (inset) in a variant of annealing twins inside the austenite matrix with no observation of SFs around them. (For interpretation of the references to colour in this figure legend, the reader is referred to the web version of this article.)

Table 2
Chemical compositions of various kinds of precipitates formed under different heat treatment conditions in several FeMnSi-SMAs and average chemical compositions of precipitates observed in this study (*).

Alloy composition (wt%)	Heat treatment	Comments	Precipitate composition (wt%)	Ref.
Fe–30Mn–6Si–5Cr	Hot-rolled	GB-phase	Fe–29.5Mn–5.9Si–6.3Cr	[70]
Fe–15Mn–7Si–9Cr–5Ni	Aged at 900 °C for 1 h	Intermetallic	Fe–17.5Mn–13.5Si–11.2Cr–7.6Ni	[71]
Fe–15Mn–6Si–9Cr–5Ni–1.5Ti–0.16C	Aged at 850 °C for 0.5 h	Rod-like	Fe–16Mn–8.5Si–10Cr–4Ni	[72]
Fe–(13–27)Mn–5.5Si–8.5Cr–5Ni	As-cast	Sigma-phase	Fe–17.7Mn–8.1Si–15.8Cr–3Ni	[73]
		Chi-phase	Fe–31.5Mn–15.8Si–7.8Cr–10.6Ni	
		Lathy-phase	Fe–12.5Mn–7Si–12.1Cr–3Ni	
Fe–17Mn–5Si–10Cr–4Ni–1(V-C)	Aged at 750 °C for 6 h	Polyhedral-shaped	Fe–14Mn–6Si–30Cr–2Ni–6V–8C	*
Fe–17Mn–5Si–10Cr–4Ni–1(V-C)	Aged at 485 °C for 6 h	Parallelogram-shaped	Fe–14Mn–5Si–26Cr–3Ni–6V–12C	*
Fe–17Mn–5Si–10Cr–4Ni–1(V-C)	Aged at 485 °C for 6 h	Elliptical-shaped	Fe–7Mn–10Cr–2Ni–50V–0.2Si –0.2C	*

aging can also stem from the segregation of solute atoms at the newly generated dislocations during aging, resulting in the local lowering of the SFE at the dislocations and causing the dislocations to dissociate to nucleate new SFs [30]. The formation of SFs in one orientation inhibits the development of new SFs in random orientations and reduces the chance of the intersection of SFs with each other. Furthermore, the increase in the size of the pre-existed V-rich particles from less than 30 nm (15–20 nm) to about 70–115 nm can have a synergistic effect on the PE improvement of the Rex-Double aged sample compared with the Rex and Rex-Aged samples.

The shape and morphology of the precipitates are determined by the interplay between the elastic strains and interfacial energy minimization during precipitation. The elastic energy is dependent on the elastic stiffness, misfit strain, precipitate size, and applied stress, and the interfacial energy is dependent on imbalanced atomic forces in the precipitate/matrix interface [57,59]. As shown in Fig. 6b, the SFs form around the polyhedral-shaped, M_7C_3-type precipitate, and after applying tensile strain they are multiplied in different orientations and trapped by the precipitate (Fig. 7a). However, the stress fields around the parallelogram-shaped, sigma-type precipitate can to some extent prevent the SFs from colliding with the precipitate (Fig. 6b), resulting in a more oriented distribution of the SFs in the austenite matrix that may reduce the probability of their trapping by the precipitate during the deformation. It should be noted that possible local chemical fluctuations in the matrix near the precipitates and their effects on local SFE variations may also influence the formation of SFs, which require further investigations in the future.

In the Rex-Aged sample with fewer oriented SFs, in comparison with the Rex-Double aged sample, multiple martensite variants form in different orientations within each austenite grain (Fig. 5d). However, due to the presence of enough large precipitates (70–330 nm) along with the higher number of oriented SFs in the Rex-Double aged sample, ε-martensite laths almost form in one orientation within each austenite grain (Fig. 6b). As a result, a relatively lower volume fraction of thermally formed ε-martensite develops in the Rex-Double aged sample (16%) compared with that of the Rex-Aged sample (43%), which may be beneficial for PE improvement because the chance of intersection between thermally formed and stress-induced formed ε-martensite is reduced.

To investigate the role of martensite-start (M_S) and austenite-start (A_S) temperatures of the $\gamma \rightleftharpoons \varepsilon$ phase transformation in the evolution of thermally formed ε-martensite, dilatometry tests were performed on the heat-treated samples. As shown in Fig. 8, the measured M_S temperatures for the Rex, Rex-Aged, and Rex-Double aged samples are 240, 255, and 260 °C, respectively, which are well above the room temperature. The increases in the M_S values after aging can be related to the formation of the precipitates and the resultant changes in the chemical composition of the austenite matrix near the precipitates and also to the lattice strains generated during the evolution of the precipitates [60–62]. Moreover, the measured A_S temperatures for the Rex, Rex-Aged, and Rex-Double aged samples are 155, 140, and 115 °C, respectively, which are lower than the corresponding M_S temperatures. These results can indicate the facilitation of martensite-to-austenite transformation by precipitation; obstacles such as precipitates can increase

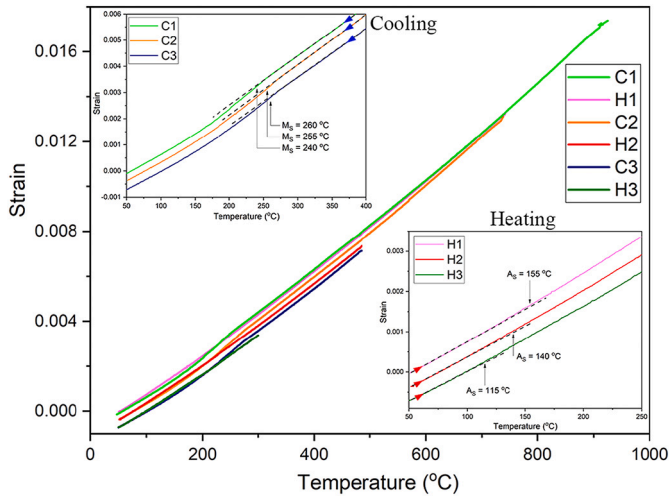

Fig. 8. Dilatation curves versus temperature at the cooling/heating rate of 1 °C/s for the Rex (C1 and H1), Rex-Aged (C2 and H2), and Rex-Double aged (C3 and H3) samples. The samples were first cooled from the heat treatment temperature and then heated to measure the γ ⇌ ε phase transformation temperatures.

the elastic energy storage during the γ → ε phase transformation, assisting the reverse transformation [63–66]. These observations suggest that the type of precipitates and the orientation of SFs are the decisive factors in determining the volume fraction of thermally formed ε-martensite in the microstructures.

Jian et al. [67] have shown that during applying strain, more SFs would form on a specific set of {111} γ planes and combine with the pre-existing SFs on these planes. The accumulation and extension of SFs on the same plane lead to the coalescence of individual SFs, generating longer SFs. The long SFs tend to be spaced regularly with the increase in the applied strain (Fig. 7a). When the spacing between adjacent long SFs reaches twice the spacing between adjacent {111} γ planes, the local regions will transform into ε-martensite. Similar to the role of precipitates, having more oriented groups of SFs may also assist in the formation of ε-martensite laths just on a specific set of {111} γ planes, thereby reducing the possibility of the intersection of ε-martensite variants with each other and consequent formation of α'-martensite, which is detrimental to PE. Additionally, the activation energy required for the γ → ε martensitic transformation is reduced by forming a high number of SFs in the matrix, resulting in better PE behavior [19]. These conditions can be met in the Rex-Double aged sample due to the formation of the sigma-type precipitates alongside the M_7C_3-type precipitates in the austenite matrix compared with the Rex-Aged sample (Figs. 6 and 7).

Another factor that improves the PE of the aged samples is the absence of coarse annealing twins in the microstructures. To obtain a good PE response, the formation of annealing twins should be suppressed in Fe–Mn–Si-based SMAs [21,68,69]. The interactions between annealing twins and stress-induced ε-martensite not only distort the twin boundaries but also significantly inhibit the γ → ε martensitic transformation. The annealing twins may also prevent the formation of thermally induced ε-martensite because a rise in the fraction of the twins lowers the M_S temperature [69].

5. Conclusions

The microstructure and pseudoelasticity (PE) of an Fe–17Mn–5Si–10Cr–4Ni–1(V-C) (wt%), Fe-based shape memory alloy have been studied under recrystallized (Rex), recrystallized and aged (Rex-Aged), and recrystallized and double aged (Rex-Double aged) conditions. According to experimental investigations and detailed microstructural and mechanical assessments, the following conclusions can be drawn:

1. The Rex specimen with a γ-austenite grain size of 5 μm has the lowest measured PE strain of 0.41% among the other specimens. Although the microstructure of the Rex specimen contains fine, equiaxed austenite grains, the presence of 7.9 vol% α'-martensite along with small V-rich particles with a size of 15–20 nm reduces the PE effect.
2. A significant improvement of approximately 20% in the PE strain is achieved by aging the Rex specimen at 750 °C for 6 h. This enhancement of PE for the Rex-Aged specimen is mainly due to the precipitation of polyhedral-shaped, (Cr–V–C)-rich precipitates (M_7C_3-type) with a uniform distribution inside the austenite grains, which causes the formation of a large number of stacking faults (SFs) and ε-martensite laths in the microstructure.
3. The highest measured PE strain of 0.77% for this alloy is attained by performing double aging heat treatment on the Rex-Aged specimen at 485 °C for 6 h. The formation of fresh, parallelogram-shaped, (Cr–V–C)-rich precipitates (sigma-type) with the average chemical composition of Fe–14Mn–5Si–26Cr–3Ni–6V–12C (wt%) and an increase in the size of pre-existed V-rich particles to 70–115 nm with the chemical composition of Fe–7Mn–10Cr–2Ni–50V–0.2Si–0.2C (wt %) are believed to be responsible for the PE improvement in the Rex-Double aged specimen.
4. The formation of sigma-type precipitates in the microstructure of the Rex-Double aged specimen causes a large number of SFs to be oriented in the same direction inside the austenite grains. It is postulated that the parallel alignment of these SFs may further improve the γ ⇌ ε martensitic phase transformation by reducing the probability of the collision of ε-martensite laths with each other and consequent formation of α'-martensite during tensile loading–unloading experiments. This results in a residual strain of 2.7% after 4% loading in tension for the Rex-Double aged specimen, which shows about 13% improvement compared with that of the Rex sample.

Declaration of Competing Interest

The authors declare that they have no known competing financial interests or personal relationships that could have appeared to influence the work reported in this paper.

Data availability

The raw/processed data required to reproduce the findings of this study are available from the corresponding authors upon reasonable request. The acquired EDS spectra used for calculating the chemical compositions of the precipitates are provided in the Supplementary Material File.

Acknowledgment

The authors acknowledge the support from re-fer AG, Switzerland, for providing the material for this research study.

Appendix A. Supplementary data

Supplementary data to this article can be found online at https://doi.org/10.1016/j.matchar.2022.112486.

References

[1] H. Koohdar, M. Nili-Ahmadabadi, F. Javadzadeh Kalahroudi, H.R. Jafarian, T. G. Langdon, The effect of high-pressure torsion on the microstructure and outstanding pseudoelasticity of a ternary Fe–Ni–Mn shape memory alloy, Mater. Sci. Eng. A 802 (2021), https://doi.org/10.1016/j.msea.2020.140647.
[2] M. Vollmer, C. Segel, P. Krooß, J. Günther, L. Tseng, On the effect of gamma phase formation on the pseudoelastic performance of polycrystalline Fe–Mn–Al–Ni shape

memory alloys, Scr. Mater. 108 (2015) 23–26, https://doi.org/10.1016/j.scriptamat.2015.06.013.
[3] A. Bauer, M. Vollmer, T. Niendorf, Effect of crystallographic orientation and grain boundaries on martensitic transformation and Superelastic response of Oligocrystalline Fe–Mn–Al–Ni shape memory alloys, Shape Mem. Superelast. 7 (2021) 373–382, https://doi.org/10.1007/S40830-021-00340-3.
[4] Z. Zhang, J. Zhang, H. Wu, Y. Ji, D. Kumar, Iron-based shape memory alloys in construction: research, applications and opportunities, Materials. 1723 (2022), https://doi.org/10.3390/ma15051723.
[5] X.L. Gu, Z.Y. Chen, Q.Q. Yu, E. Ghafoori, Stress recovery behavior of an Fe-Mn-Si shape memory alloy, Eng. Struct. 243 (2021), 112710, https://doi.org/10.1016/J.ENGSTRUCT.2021.112710.
[6] H. Peng, G. Wang, S. Wang, J. Chen, I. MacLaren, Y. Wen, Key criterion for achieving giant recovery strains in polycrystalline Fe-Mn-Si based shape memory alloys, Mater. Sci. Eng. A 712 (2018) 37–49, https://doi.org/10.1016/j.msea.2017.11.071.
[7] A.V. Druker, A. Perotti, I. Esquivel, J. Malarría, A manufacturing process for shaft and pipe couplings of Fe–Mn–Si–Ni–Cr shape memory alloys, Mater. Des. 56 (2014) 878–888, https://doi.org/10.1016/j.matdes.2013.11.032.
[8] W.J. Lee, B. Weber, C. Leinenbach, Recovery stress formation in a restrained Fe–Mn–Si-based shape memory alloy used for prestressing or mechanical joining, Constr. Build. Mater. 95 (2015) 600–610, https://doi.org/10.1016/J.CONBUILDMAT.2015.07.098.
[9] L. Janke, C. Czaderski, M. Motavalli, J. Ruth, Applications of shape memory alloys in civil engineering structures—overview, limits and new ideas, Mater. Struct. 38 (5) (2005) 578–592, https://doi.org/10.1007/BF02479550.
[10] H. Otsuka, K. Nakajima, T. Maruyama, Superelastic behavior of Fe–Mn–Si–Cr shape memory alloy coil, Mater. Trans. 41 (2000) 547–549, https://doi.org/10.2320/MATERTRANS1989.41.547.
[11] Z. Dong, U.E. Klotz, C. Leinenbach, A. Bergamini, C. Czaderski, M. Motavalli, A novel Fe-Mn-Si shape memory alloy with improved shape recovery properties by VC precipitation, Adv. Eng. Mater. 11 (2009) 40–44, https://doi.org/10.1002/adem.200800312.
[12] W. Wang, A. Hosseini, E. Ghafoori, Experimental study on Fe-SMA-to-steel adhesively bonded interfaces using DIC, Eng. Fract. Mech. 244 (2021), 107553, https://doi.org/10.1016/J.ENGFRACMECH.2021.107553.
[13] E. Ghafoori, M. Neuenschwander, M. Shahverdi, C. Czaderski, M. Fontana, Elevated temperature behavior of an iron-based shape memory alloy used for prestressed strengthening of civil structures, Constr. Build. Mater. 211 (2019) 437–452, https://doi.org/10.1016/J.CONBUILDMAT.2019.03.098.
[14] D.I.H. Rosa, A. Hartloper, A. de Castro e Sousa, D.G. Lignos, M. Motavalli, E. Ghafoori, Experimental behavior of iron-based shape memory alloys under cyclic loading histories, Constr. Build. Mater. 272 (2021), 121712, https://doi.org/10.1016/J.CONBUILDMAT.2020.121712.
[15] E. Hosseini, E. Ghafoori, C. Leinenbach, M. Motavalli, S.R. Holdsworth, Stress recovery and cyclic behaviour of an Fe–Mn–Si shape memory alloy after multiple thermal activation, Smart Mater. Struct. 27 (2018), 025009, https://doi.org/10.1088/1361-665X/AAA2C9.
[16] C. Leinenbach, H. Kramer, C. Bernhard, D. Eifler, Thermo-mechanical properties of an Fe–Mn–Si–Cr–Ni–VC shape memory alloy with low transformation temperature, Adv. Eng. Mater. 14 (2012) 62–67, https://doi.org/10.1002/adem.201100129.
[17] J. Vůjtěch, P. Ryjáček, J.C. Matos, E. Ghafoori, Iron-based shape memory alloy for strengthening of 113-year bridge, Eng. Struct. 248 (2021), 113231, https://doi.org/10.1016/j.engstruct.2021.113231.
[18] R. Fosdick, Y. Ketema, Shape memory alloys for passive vibration damping, J. Intell. Mater. Syst. Struct. 9 (1998) 854–870, https://doi.org/10.1177/1045389X9800901009.
[19] C. Leinenbach, A. Arabi-Hashemi, W.J. Lee, A. Lis, M. Sadegh-Ahmadi, S. van Petegem, T. Panzner, H. van Swygenhoven, Characterization of the deformation and phase transformation behavior of VC-free and VC-containing FeMnSi-based shape memory alloys by in situ neutron diffraction, Mater. Sci. Eng. A 703 (2017) 314–323, https://doi.org/10.1016/j.msea.2017.07.077.
[20] T. Omori, M. Okano, R. Kainuma, Effect of grain size on superelasticity in Fe-Mn-Al-Ni shape memory alloy wire, APL Mater. 1 (2013), https://doi.org/10.1063/1.4820429.
[21] G. Wang, H. Peng, C. Zhang, S. Wang, Y. Wen, Relationship among grain size, annealing twins and shape memory effect in Fe–Mn–Si based shape memory alloys, Smart Mater. Struct. 25 (2016), 075013, https://doi.org/10.1088/0964-1726/25/7/075013.
[22] A. Arabi-Hashemi, W.J. Lee, C. Leinenbach, Recovery stress formation in FeMnSi based shape memory alloys: impact of precipitates, texture and grain size, Mater. Des. 139 (2018) 258–268, https://doi.org/10.1016/j.matdes.2017.11.006.
[23] O. Matsumura, T. Sumi, N. Tamura, K. Sakao, T. Furukawa, H. Otsuka, Pseudoelasticity in an Fe–28Mn–6Si–5Cr shape memory alloy, Mater. Sci. Eng. A 279 (2000) 201–206, https://doi.org/10.1016/S0921-5093(99)00644-9.
[24] Y.H. Wen, L.R. Xiong, N. Li, W. Zhang, Remarkable improvement of shape memory effect in an Fe–Mn–Si–Cr–Ni–C alloy through controlling precipitation direction of Cr23C6, Mater. Sci. Eng. A 474 (2008) 60–63, https://doi.org/10.1016/J.MSEA.2007.05.043.
[25] N. Stanford, D.P. Dunne, Effect of NbC and TiC precipitation on shape memory in an iron-based alloy, J. Mater. Sci. 41 (2006) 4883–4891, https://doi.org/10.1007/S10853-006-0050-7.
[26] K. Li, Z. Dong, Y. Liu, L. Zhang, A newly developed Fe-based shape memory alloy suitable for smart civil engineering, Smart Mater. Struct. 22 (2013), 045002, https://doi.org/10.1088/0964-1726/22/4/045002.
[27] L. Chengxin, W. Guixin, W. Yandong, L. Qingsuo, Z. Jianjun, Effect of addition of V and C on strain recovery characteristics in Fe–Mn–Si alloy, Mater. Sci. Eng. A 438–440 (2006) 808–811, https://doi.org/10.1016/J.MSEA.2006.01.098.
[28] S. Kajiwara, D. Liu, T. Kikuchi, N. Shinya, Remarkable improvement of shape memory effect in Fe-Mn-Si based shape memory alloys by producing NbC precipitates, Scr. Mater. 44 (2001) 2809–2814, https://doi.org/10.1016/S1359-6462(01)00978-2.
[29] A. Baruj, T. Kikuchi, S. Kajiwara, N. Shinya, Improvement of shape memory properties of NbC containing Fe–Mn–Si based shape memory alloys by simple thermomechanical treatments, Mater. Sci. Eng. A 378 (2004) 333–336, https://doi.org/10.1016/j.msea.2003.10.357.
[30] M.J. Lai, Y.J. Li, L. Lillpopp, D. Ponge, S. Will, D. Raabe, On the origin of the improvement of shape memory effect by precipitating VC in Fe–Mn–Si-based shape memory alloys, Acta Mater. 155 (2018) 222–235, https://doi.org/10.1016/j.actamat.2018.06.008.
[31] J. van Aswegen, R.D.W. Honeycombe, Precipitation on stacking faults in Cr-Ni austenitic steels, Acta Metall. 12 (1965) 1–13, https://doi.org/10.1016/0001-6160(64)90048-3.
[32] F.H. Froes, B.W.K. Honeycombe, D.H. Warrington, Conditions controlling matrix and stacking fault precipitation, Acta Metall. 15 (1967) 157–159, https://doi.org/10.1016/0001-6160(67)90170-8.
[33] K. Kamei, Y. Maehara, Y. Ohmori, Effect of stacking fault precipitation on hot deformation of austenitic stainless steel, Trans. Iron Steel Inst. Jpn. 26 (1986) 159–166, https://doi.org/10.2355/ISIJINTERNATIONAL1966.26.159.
[34] J.J. Irani, R.T. Weiner, Precipitation of vanadium carbide on stacking faults, Nature 205 (4973) (1965) 795, https://doi.org/10.1038/205795a0.
[35] H. Khodaverdi, M. Mohri, E. Ghafoori, A. Sabet Ghorabaei, M. Nili-Ahmadabadi, Enhanced pseudoelasticity of an Fe–Mn–Si-based shape memory alloy by applying microstructural engineering through recrystallization and precipitation, J. Mater. Res. Technol. 21C (2022) 2999–3013, https://doi.org/10.1016/j.jmrt.2022.10.092.
[36] M. Mohri, I. Ferretto, C. Leinenbach, D. Kim, D.G. Lignos, E. Ghafoori, Effect of thermomechanical treatment and microstructure on pseudo-elastic behavior of Fe–Mn–Si–Cr–Ni-(V, C) shape memory alloy, Mater. Sci. Eng. A 855 (2022), 143917, https://doi.org/10.1016/J.MSEA.2022.143917.
[37] G. Cliff, G.W. Lorimer, The quantitative analysis of thin specimens, J. Microsc. 103 (1975) 203–207, https://doi.org/10.1111/j.1365-2818.1975.tb03895.x.
[38] Thermo-Calc Documentation Set, Version, 2022.
[39] T. Song, B.C. de Cooman, Martensite nucleation at grain boundaries containing intrinsic grain boundary dislocations, ISIJ Int. 54 (2014) 2394–2403, https://doi.org/10.2355/ISIJINTERNATIONAL.54.2394.
[40] M.J. Sohrabi, M. Naghizadeh, H. Mirzadeh, Deformation-induced martensite in austenitic stainless steels: a review, Arch. Civil Mech. Eng. 20 (2020) 1–24, https://doi.org/10.1007/s43452-020-00130-1.
[41] J.H. Robertson, IUCr, Elements of X-ray Diffraction by B. D. Cullity, Urn:Issn:0567-7394 35, 1979, p. 350, https://doi.org/10.1107/S0567739479000917, 1-509.
[42] M.M. Pan, X.M. Zhang, D. Zhou, R.D.K. Misra, P. Chen, Fe–Mn–Si–Cr–Ni based shape memory alloy: thermal and stress-induced martensite, Mater. Sci. Eng. A 797 (2020), https://doi.org/10.1016/j.msea.2020.140107.
[43] G. Nolze, PowderCell: A Mixture between Crystal Structure Visualizer, Simulation and Refinement Tool, International School on Powder Diffraction, 2002.
[44] W.J. Lee, B. Weber, G. Feltrin, C. Czaderski, M. Motavalli, C. Leinenbach, Phase transformation behavior under uniaxial deformation of an Fe–Mn–Si–Cr–Ni–VC shape memory alloy, Mater. Sci. Eng. A 581 (2013) 1–7, https://doi.org/10.1016/j.msea.2013.06.002.
[45] M. Beßling, C. Czaderski, J. Orlowsky, Prestressing effect of shape memory alloy reinforcements under serviceability tensile loads, Buildings 11 (2021) (2021) 101, https://doi.org/10.3390/buildings11030101.
[46] T. Sawaguchi, T. Kikuchi, S. Kajiwara, The pseudoelastic behavior of Fe–Mn–Si-based shape memory alloys containing Nb and C, Smart Mater. Struct. 14 (2005) S317, https://doi.org/10.1088/0964-1726/14/5/022.
[47] N. Bergeon, G. Guenin, C. Esnouf, Microstructural analysis of the stress-induced ε martensite in a Fe–Mn–Si–Cr–Ni shape memory alloy: part I—calculated description of the microstructure, Mater. Sci. Eng. A 242 (1998) 77–86, https://doi.org/10.1016/S0921-5093(97)00511-X.
[48] N. Bergeon, G. Guenin, C. Esnouf, Microstructural analysis of the stress-induced ε martensite in a Fe–Mn–Si–Cr–Ni shape memory alloy: part II: transformation reversibility, Mater. Sci. Eng. A 242 (1998) 87–95, https://doi.org/10.1016/S0921-5093(97)00512-1.
[49] E. Gartstein, A. Rabinkin, On the f.c.c. → h.c.p. phase transformation in high manganese-iron alloys, Acta Metall. 27 (1979) 1053–1064, https://doi.org/10.1016/0001-6160(79)90193-7.
[50] H. Li, D. Dunne, N. Kennon, Factors influencing shape memory effect and phase transformation behaviour of Fe–Mn–Si based shape memory alloys, Mater. Sci. Eng. A 273–275 (1999) 517–523, https://doi.org/10.1016/S0921-5093(99)00391-3.
[51] S. Kajiwara, Characteristic features of shape memory effect and related transformation behavior in Fe-based alloys, Mater. Sci. Eng. A 273 (1999) 67–88, https://doi.org/10.1016/S0921-5093(99)00290-7.
[52] L. Bracke, L. Kestens, J. Penning, Transformation mechanism of α'-martensite in an austenitic Fe–Mn–C–N alloy, Scr. Mater. 57 (2007) 385–388, https://doi.org/10.1016/j.scriptamat.2007.05.003.
[53] N. Stanford, D.P. Dunne, Effect of second-phase particles on shape memory in Fe–Mn–Si-based alloys, Mater. Sci. Eng. A 454 (2007) 407–415, https://doi.org/10.1016/j.msea.2006.11.084.

[54] Y. Chen, T. Burgess, X. An, Y.-W. Mai, H.H. Tan, J. Zou, S.P. Ringer, C. Jagadish, X. Liao, Effect of a high density of stacking faults on the Young's modulus of GaAs nanowires, Nano Lett. 16 (2016) 1911–1916, https://doi.org/10.1021/acs.nanolett.5b05095.
[55] A.I. Gorunov, Investigation of M7C3, M23C6 and M3C carbides synthesized on austenitic stainless steel and carbon fibers using laser metal deposition, Surf. Coat. Technol. 401 (2020), 126294, https://doi.org/10.1016/J.SURFCOAT.2020.126294.
[56] F. Ernst, D. Li, H. Kahn, G.M. Michal, A.H. Heuer, The carbide M7C3 in low-temperature-carburized austenitic stainless steel, Acta Mater. 59 (2011) 2268–2276, https://doi.org/10.1016/J.ACTAMAT.2010.11.058.
[57] R. Shi, N. Ma, Y. Wang, Predicting equilibrium shape of precipitates as function of coherency state, Acta Mater. 60 (2012) 4172–4184, https://doi.org/10.1016/J.ACTAMAT.2012.04.019.
[58] J.R. Patel, K.A. Jackson, H. Reiss, Oxygen precipitation and stacking-fault formation in dislocation-free silicon, J. Appl. Phys. 48 (2008) 5279, https://doi.org/10.1063/1.323558.
[59] A.M. Jokisaari, S.S. Naghavi, C. Wolverton, P.W. Voorhees, O.G. Heinonen, Predicting the morphologies of γ' precipitates in cobalt-based superalloys, Acta Mater. 141 (2017) 273–284, https://doi.org/10.1016/J.ACTAMAT.2017.09.003.
[60] D.L. Rittermann, A. Kyrolainen, P.J. Ferreira, Influence of annealing treatment on the formation of nano/submicron grain size AISI 301 Austenitic stainless steels, Metall. Mater. Trans. A 37 (8) (2006) 2325–2338, https://doi.org/10.1007/BF02586207.
[61] A. Sato, K. Soma, T. Mori, Hardening due to pre-existing ϵ-Martensite in an Fe-30Mn-1Si alloy single crystal, Acta Metall. 30 (1982) 1901–1907, https://doi.org/10.1016/0001-6160(82)90030-X.
[62] V. Kokorin, L. Kozlova, A. Titenko, Temperature hysteresis of martensite transformation in aging Cu–Mn–Al alloy, Scr. Mater. 47 (2002) 499–502, https://doi.org/10.1016/S1359-6462(02)00136-7.
[63] D.P. Dunne, C.M. Wayman, The effect of austenite ordering on the martensite transformation in Fe-Pt alloys near the composition Fe3Pt: I. Morphology and transformation characteristics, Metall. Trans. A. 4 (1) (1973) 137–145, https://doi.org/10.1007/BF02649612.
[64] D.P. Dunne, C.M. Wayman, The effect of austenite ordering on the martensite transformation in Fe-Pt alloys near the composition Fe3Pt: II. Crystallography and general features, Metall. Trans. A. 4 (1) (1973) 147–152, https://doi.org/10.1007/BF02649613.
[65] E. Acar, G.P. Toker, H. Kurkcu, H.E. Karaca, High temperature shape memory behavior of Ni47.3Ti29.7Hf20Pd3 alloys, Intermetallics (Barking) 111 (2019), 106518, https://doi.org/10.1016/J.INTERMET.2019.106518.
[66] E. Acar, M. Kok, I.N. Qader, Exploring surface oxidation behavior of NiTi–V alloys, Eur. Phys. J. Plus 135 (1) (2020) 1–9, https://doi.org/10.1140/EPJP/S13360-019-00087-Y.
[67] L. Jian, C.M. Wayman, On the mechanism of the shape memory effect associated with γ(fcc) to ε(hcp) martensitic transformations in Fe-Mn-Si based alloys, Scr. Metall. Mater. 27 (1992) 279–284, https://doi.org/10.1016/0956-716X(92)90512-D.
[68] H. Peng, G. Wang, Y. Du, S. Wang, J. Chen, Y. Wen, A novel training-free processed Fe-Mn-Si-Cr-Ni shape memory alloy undergoing δ → γ phase transformation, Metall. Mater. Trans. A Phys. Metall. Mater. Sci. 47 (2016) 3277–3283, https://doi.org/10.1007/S11661-016-3521-8.
[69] Y.H. Wen, H.B. Peng, D. Raabe, I. Gutierrez-Urrutia, J. Chen, Y.Y. Du, Large recovery strain in Fe-Mn-Si-based shape memory steels obtained by engineering annealing twin boundaries, Nat. Commun. 5 (1) (2014) 1–9, https://doi.org/10.1038/ncomms5964.
[70] H. Lin, C. Lin, K. Lin, Y. Chuang, An investigation of grain-boundary phase in Fe–30Mn–6Si–5Cr shape memory alloy, J. Alloys Compd. 27 (2001) 279–284.
[71] B. Maji, M. Krishnan, The effect of microstructure on the shape recovery of a Fe–Mn–Si–Cr–Ni stainless steel shape memory alloy, Scr. Mater. 48 (2003) 71–77, https://doi.org/10.1016/S1359-6462(02)00348-2.
[72] D. Bu, H. Peng, Y. Wen, N. Li, Influence of ageing on wear resistance of an Fe–Mn–Si–Cr–Ni–Ti–C shape memory alloy, Mater. Des. 32 (2011) 2969–2973, https://doi.org/10.1016/j.msea.2017.11.071.
[73] H. Peng, Y. Wen, Y. Du, Q. Yu, Q. Yang, Effect of manganese on microstructures and solidification modes of cast Fe-Mn-Si-Cr-Ni shape memory alloys, Metall. Mater. Trans. B Process Metall. Mater. Process. Sci. 44 (2013) 1137–1143, https://doi.org/10.1007/S11663-013-9880-2.